RESEARCH ARTICLE

Wall shear stress during impingement at the building platform can exceed nozzle wall shear stress in microvalve-based bioprinting

Ramin Nasehi, Sanja Aveic, Horst Fischer*

Department of Dental Materials and Biomaterials Research, RWTH Aachen University Hospital, Aachen, Germany

*Corresponding author:
Horst Fischer
(hfischer@ukaachen.de)

Abstract

It is well known that in microvalve-based bioprinting, the cells are subjected to wall shear stress, which can negatively affect their viability rate. We hypothesized that the wall shear stress during impingement at the building platform, hitherto not considered in microvalve-based bioprinting, can be even more critical for the processed cells than the wall shear stress inside the nozzle. To test our hypothesis, we used fluid mechanics numerical simulation based on finite volume method. In addition, viability of two functionally different cell types, HaCaT cell line and primary human umbilical vein endothelial cells (HUVECs), embedded in the cell-laden hydrogel was assessed after bioprinting. Simulation results revealed that at low upstream pressure the kinetic energy was not sufficient to overcome the interfacial force for droplet formation and detachment. Oppositely, at relatively mid upstream pressure, a droplet and a ligament were formed, whereas at higher upstream pressure, a jet was formed between nozzle and platform. In the case of jet formation, the shear stress during impingement can exceed the wall shear stress in the nozzle. The amplitude of impingement shear stress depended on nozzle-to-platform distance. This was confirmed by evaluating cell viability which revealed an increase of up to 10% when increasing the nozzle-to-platform distance from 0.3 to 3 mm. In conclusion, the impingement-related shear stress can exceed the wall shear stress in the nozzle in microvalve-based bioprinting. However, this critical issue can be successfully addressed by adapting the distance between the nozzle and the building platform. Altogether, our results highlight impingement-related shear stress as another essential parameter to consider in devising bioprinting strategies.

Keywords: Bioprinting; Wall shear stress; Cell viability; Fluid mechanics; Numerical simulation

1. Introduction

Several bioprinting methods have become established, including microextrusion[1], inkjet[2], microvalve-based[3], vat polymerization-based[4], laser-based[5,6], and acoustic[7] bioprinting. These methods vary in physical principle, printing resolution, and mechanical stimulation, all of which affect the processed cells[8,9]. The choice of both bioink and method is usually made based on application[10]. In the view of standardization

of process terminology, Lee *et al.*[11] proposed four categories of bioprinting technologies: material jetting, vat photopolymerization, material extrusion, and free-form spatial printing. In the case of nozzle-based bioprinting methods, the mechanical stimuli become extreme by the increase of required resolution. In inkjet bioprinting, the droplet ejection relies on a pressure pulse distributed in the bioink chamber to form and transfer a droplet to the platform. Derby[12] showed that for the drop ejection of a Newtonian fluid, materials can be benchmarked based on their rheological properties in accordance with the values of three dimensionless parameters: Reynolds ($Re = \rho v d/\mu$), Weber ($We = \rho v^2 d/\sigma$), and Ohnesorge ($Oh = \sqrt{We}/Re$) numbers. Yet, most bioinks exhibit viscoelastic behavior that makes it difficult to directly benchmark them into printable and not printable material based on the study cited. Gudapati *et al.*[13,14] showed that collagen, fibrinogen, and thrombin can be printed dropwise only at a certain protein concentration and using certain nozzle sizes. Moreover, they showed that the addition of a non-ionic surfactant prevents the formation of the interfacial layer, which consequently helps to resolve the inconsistencies in rheological measurements and bioprinting. Xu *et al.*[15] used alginate solution and identified four break-up types based on ligament pinch-off position depending on the alginate concentration. These studies focused on the dispensing dynamics of the nozzle of piezoelectric microvalves, while leaving the question of its effect on and interaction with the living cells unexplored.

In principle, the method-immanent mechanical stimuli on the processed cells are determinant factors for a successful bioprinting[16,17]. It has been shown that bioprinting-associated shear stress has an adverse effect on cell viability[18,19] during the printing process that eventually causes limited integrity and functionality of the cells post-printing[20,21]. Some studies[16,17,22] have used numerical simulation to determine the shear stress involved in microextrusion bioprinting and discussed solutions for minimizing this since it is considered a detrimental effect associated to the bioprinting. In droplet-based techniques, another source of mechanical stress on cells is the impingement shear stress that has been studied partly in laser-induced forward transfer bioprinting[23,24]. However, there is less known about the mechanical effect on the cells due to impingement onto the building platform during microvalve bioprinting. We hypothesized that the impingement effect can be even more critical for the cells due to higher shear stresses compared to the wall shear stresses occurring during droplet ejection inside the nozzle tip. To test this hypothesis, we considered alginate 1.5% w/v as an optimal bioink for our study because it exhibits the shear-thinning behavior recommended for bioinks in

order to minimize the nozzle wall shear stress[17,25]. To elaborate the dispensing dynamics and to calculate the wall shear stress, as well as the shear stress during impingement of the cell-laden droplet at the building platform, we used a finite volume method-based simulation model using commercial software Ansys Fluent 2021 R2. In addition, we verified and validated *in vitro* the findings from the *in silico* simulation by performing cell viability analysis after dispensing cell-laden alginate from several nozzle-to-platform distances. Two functionally diverse cell types (HaCaT epithelial cell line and primary human umbilical vein endothelial cells [HUVECs]) were considered.

2. Materials and methods

2.1. Numerical simulation

Ansys Fluent 2021 R2 was used for the numerical simulations. For this purpose, a multi-phase laminar model based on volume of fluid method considering continuum surface force, as for phase interaction, was chosen. The fluids were assumed to be incompressible, isothermal condition was imposed, and the maximum root mean square (RMS) residual error of 10^{-3} was chosen. We set a Pressure-Implicit with Splitting of Operators (PISO) scheme for pressure-velocity coupling. Least squares cell-based, body force weighted, second-order upwind, and compressive methods were used for spatial discretization of gradients, pressure, momentum, and volume fraction terms, respectively. For transient terms, first-order implicit method was used. As for the geometry, the nozzle size of mechanical microvalves (SMLD 300G, Fritz Gyger AG, Gwatt, Switzerland; nozzle diameters 150 μm and 300 μm) was considered for the simulations. This valve consists of a stationary piston, a moving piston, and a spring that ensures microvalve closure. By imposing a high upstream pressure, the cell suspension is placed under pressure, and as soon as the valve opens, a drop is ejected. For the numerical simulation, a non-uniform mesh with semi-structured grids grown from wall surfaces (boundary layer meshes) was generated. A grid study was performed on at least three cases of fine, medium, and coarse meshes considering the maximum wall shear stress as the sensitive parameter. Transient simulation was performed considering a valve opening time of 400 μs. More information regarding the geometry, boundary conditions, meshing, and numerical model is presented in **Supplementary File**.

2.2. Experimental setup

To capture the droplet ejection dynamic, a custom-made experimental setup was built. This setup was based on a drop-on-demand (DoD) bioprinter previously custom-made in our lab. In this setup, the position of the solenoid microvalve (SMLD 300G, Fritz Gyger AG,

Gwatt, Switzerland; nozzle diameter 300 μm) was fixed, while the position of the platform in two horizontal and vertical directions was adjustable. The following printing parameters were used for cell-laden alginate droplet ejection: 10 droplets per printing position, either 0.6 or 1.0 bar upstream hydrostatic pressure, and microvalve opening time of 400 μs.

2.3. Hydrogel preparation
Alginate 1.5% wt/v was prepared by dissolving the respective amount of alginic acid sodium salt (Sigma-Aldrich, St. Louis, USA) overnight in deionized water (for the cell-free experiments) on the roller at room temperature. For the experiment including the cells, 2% w/v alginate solution was prepared by rolling HaCaT/HUVECs culture medium rolling overnight at room temperature. Later on, the solution was diluted and mixed with cell suspension to a final concentration of 1.5% w/v and 2×10^6 cells/mL.

2.4. Viscosity measurement
Viscosity data were used as input for the simulation of the alginate fluid flow. Viscosity measurements were performed by rotary rheometer (Kinexus ultra+, Malvern Instruments Ltd., Malvern, UK) using a 0.5° cone geometry. The shear rate was continuously increased according to a defined range from 0.1 to at least 10,000 s^{-1} within a period of 20 min, during which the viscosity and shear stress were measured.

2.5. Time lapse imaging using high-speed camera (HSC)
Droplet formation and impinging dynamics were captured using PASTCAM Mini AX50 (Photron, Tokyo, Japan) and a custom-made droplet ejection setup using SMLD 300G microvalves. A shutter speed of 1/18,000 s and frame rate of 10,000 fps were used. Image resolution was 256 × 128 pixels. Image processing was done by ImageJ software (National Institutes of Health, Bethesda, USA).

2.6. Cell lines and primary cells
Immortalized human HaCaT keratinocytes were kindly provided by Prof. P. Boukamp[26]. The cells were cultured in Dulbecco's Modified Eagle Medium (DMEM) GlutaMax (Thermo Fisher Scientific, Waltham, USA) supplemented with 10% fetal calf serum and 1% penicillin/streptomycin (PAN-Biotech, Aidenbach, Germany). Cells were passaged 2–3 days after reaching confluence as follows: The medium was removed from the flask, and 5 mL of phosphate-buffered saline (PBS) without Ca^{2+}/Mg^{2+} was added to wash the residual medium. Then, cells were incubated with fresh PBS in 5% CO_2 at 37°C for 20 min. The PBS was carefully removed, and 1 mL of 0.05% trypsin–0.02% ethylenediaminetetraacetic acid (EDTA) solution (Pan Biotech) was added and incubated again at 37°C for 10 min, after which 4 mL of culture medium was added to

stop the trypsin–EDTA reaction. The cell suspension was then transferred to a 15 mL conical tube and centrifuged at $300 \times g$ for 3 min. The supernatant was carefully removed, and cells were re-suspended in 5 mL of fresh, pre-warmed culture medium and seeded onto new T25 culture flasks with a split ratio of 1:5.

Primary HUVECs were isolated from umbilical cords provided by the Department of Gynecology and Perinatal Medicine, RWTH Aachen University Hospital, Aachen, Germany, as approved by the local ethics committee of the Faculty of Medicine at RWTH Aachen University (EK 424/19). Briefly, the umbilical cords were rinsed in PBS for 5 min. In order to remove coagulated blood, the veins were flushed with PBS and then filled with collagenase solution (collagenase type I, 400 U/mL, dissolved in Hank's Balanced Salt Solution with $CaCl_2$ and $MgCl_2$, both Gibco by Life Technologies, USA) and closed with a clip at both ends. The umbilical cord was then placed on a petri dish and incubated for 30 min (37°C and 5% CO_2). The clips were then removed, and fresh PBS was used to flush the vein. The cell suspension was collected in a Falcon tube and centrifuged ($300 \times g$ for 5 min; CT6EL, Hitachi Koki, Tokyo, Japan). The supernatant was removed from the tube, and the remaining cell pellet was suspended with 10 mL of endothelial cell basal medium (C-22111, PromoCell, Heidelberg, Germany). The cells were transferred to gelatin-coated cell culture flasks (2% gelatin from porcine skin, gel strength 300, Type A, Sigma-Aldrich, St. Louis, USA) and incubated at 37°C and 5% CO_2. The cells were cultured up to fifth passage.

2.7. Live-dead staining and immunofluorescence imaging
An alginate solution with final concentration of 1.5% w/v containing 2×10^6 cells/mL (HUVEC or HaCaT) was prepared. The live-dead staining solution was prepared by mixing 2.5 μL of both fluorescein diacetate (FDA; Sigma-Aldrich, St. Louis, USA) and propidium iodide (PI; 94% HPLC, Sigma-Aldrich, St. Louis, USA) into 125 μL of Ringer's solution, and kept away from light. The cell-alginate suspension was transferred to the custom-made cartridge for droplet ejection. Then, the cell suspension was dispensed through a solenoid microvalve (SMLD 300G, Fritz Gyger, Gwatt, Switzerland; valve diameter 300 μm) at two different upstream pressures of 1.0 ± 0.1 bar or 0.6 ± 0.1 bar with an opening time of 400 μs. The distance from the nozzle tip to the platform (microscope glass) varied from 0.3 ± 0.06 mm to 3.0 ± 0.06 mm. At each nozzle-to-platform distance, ten droplets were ejected on the platform. Subsequently, the same volume of live-dead staining solution was pipetted on top of ejected droplet. The samples were then covered with a round cover slip. Imaging was performed using a
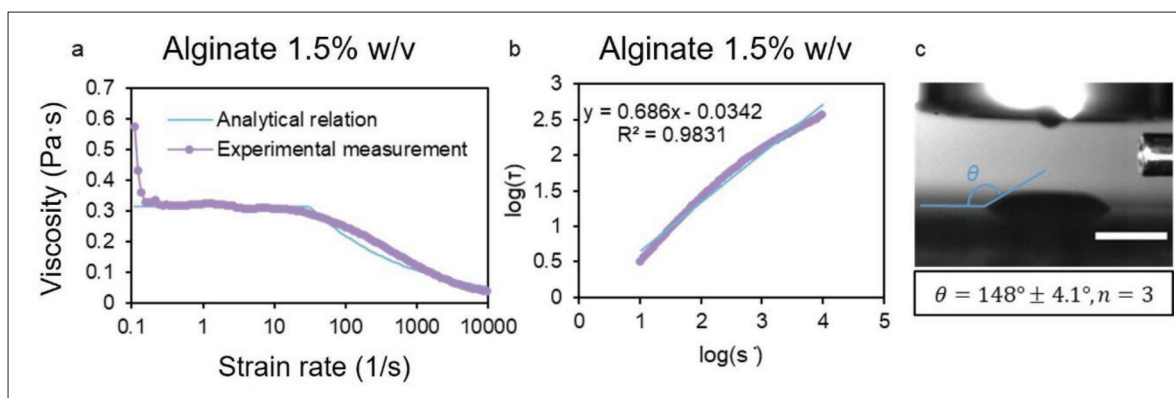
Figure 1. The viscosity of alginate 1.5% wt/v was measured using a rotary rheometer at strain rates ranging from 0.1 to 5000 s⁻¹ (a). Based on Equation II-b, a linear function was matched to the experimental measurements in strain rates ranging from 30 to 50,000 s⁻¹ (b). The contact angle of alginate 1.5% w/v was measured by calculating the angle between substrate and droplet surface after ejection from the nozzle using ImageJ software (c). The scale bar represents 1 mm.

fluorescence microscope (Axio Imager M2M, Carl Zeiss, Oberkochen, Germany) at five-fold magnification. For each sample, the images were taken at three different positions. Non-ejected cell-alginate suspension that was taken from the cartridge was used as control.

2.8. Image analysis

All image analysis was done using ImageJ software (National Institutes of Health, Bethesda, MD, USA). For viability analysis of fluorescence images, first 8-bit images were prepared. Then, after defining a proper threshold, the images were converted to binary black and white images. To split the separate cells, the Watershed tool was used. Then, the number of cells in each channel was measured using ImageJ's Analyze Particles tool (National Institutes of Health, Bethesda, MD, USA). The live and dead cell counts were stored in an Excel file, and the percentage of dead cells was calculated using the following formula:

$$\% \text{ Dead cells} = \frac{\text{Number of dead cells}}{\text{Total number of cells}} \times 100 \qquad (I)$$

2.9. Statistical analysis

Data were obtained from at least three independent experiments. Statistical evaluation was performed on the raw data. The results are presented as mean ± standard deviation (SD). One-way analysis of variance (ANOVA) followed by Tukey's Multiple Comparison (GraphPad Prism 9.1.1 software) was used. The differences were considered significant at $*p < 0.05$, $**p < 0.01$, $***p < 0.001$, and $****p < 0.0001$.

3. Results

3.1. Viscosity and contact angle of alginate solution

Figure 1a shows the viscosity of alginate 1.5% w/v versus strain rate in the range of 0.1 to 10.000 s⁻¹ in logarithmic

Table 1. Values of the parameters involved in Equation II-c for modeling alginate viscosity

Parameter	$\dot{s}_{min}$ (s⁻¹)	$\dot{s}_{max}$ (s⁻¹)	μ_{min} (Pa·s)	μ_{max} (Pa·s)	k (Pa·sⁿ)	n
Value	30	50,000	0.03	0.315	0.924272	0.686

scale. In our measurements, alginate behaved like a Newtonian fluid at small strain rates (bellow 30 s⁻¹), but as the strain rate increased, it behaved as a shear-thinning material. Therefore, a multi-function power-law model, Equation II, was used to analytically estimate the alginate viscosity.

$$\tau = \mu \dot{s} = k\dot{s}^n \qquad (II\text{-}a)$$

$$\log \tau = \log k + n \log \dot{s} \qquad (II\text{-}b)$$

$$\mu = \begin{cases} \mu_{\max}, & \dot{s} < \dot{s}_{\min} \\ k\dot{s}^{n-1}, & \dot{s}_{\min} \leq \dot{s} \leq \dot{s}_{\max} \\ \mu_{\min}, & \dot{s}_{\max} < \dot{s} \end{cases} \qquad (II\text{-}c)$$

In this equation, τ is the shear stress (Pa), μ is the viscosity (Pa·s), and $\dot{s}$ is the strain rate (s⁻¹). The flow consistency index (k) and power-law index (n) were calculated based on a linear function fitted to experimental measurements with $R^2 \cong 0.98$ (Equation II-b and Figure 1b). The respective values of parameters extracted from the analytical model (Equation II-c) fit to experimental data are summarized in Table 1. These values were used later in the numerical model. The contact angle of alginate 1.5% w/v was measured from the images obtained by HSC for three different drop sizes (Figure 1c). The contact angle was $\theta = 148.0° \pm 4.1°$ and was used in the numerical model.

3.2. Validation and verification of simulation model

The simulation model was validated by comparing the dispensing dynamic predicted by simulation with that
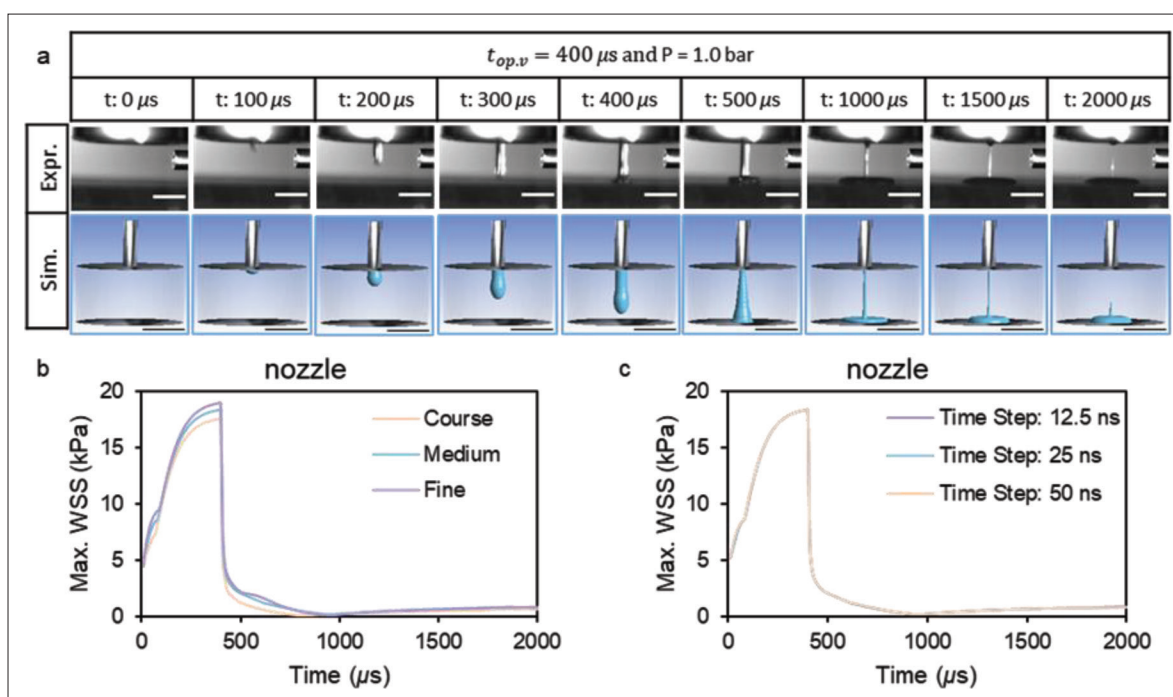
Figure 2. Validation of the simulation model. (a) Simulation model predicts dispensing dynamics similar to that captured by HSC during 2000 μs. Scale bar: 1 mm. (b) Maximum wall shear stress inside the nozzle varies slightly by different mesh sizes (course, medium, and fine). Medium mesh size was used for follow-up simulations. (c) Similar maximum wall shear stress inside the nozzle was predicted by numerical simulation using different time steps of 12.5, 25, and 50 ns (results are overlapped). Therefore, 25 ns was used for follow-up simulations.

captured by HSC. The experiment was conducted using a SMLD 300G-300 μm microvalve. The opening time of the valve was set to 400 μs with an upstream pressure of 1.0 ± 0.1 bar. The distance between the platform and nozzle was set to 1.20 ± 0.06 mm in the experiment. These same values were implemented in the simulation model (details of the geometry and numerical model are described in section 2 and **Supplementary File**). The simulation results predicted a droplet/jet formation dynamic similar to that captured by HSC during the experiment (Figure 2a; **Videoclips S1** and **S2** in Supplementary File). A total time of 2000 μs was considered. Furthermore, the sensitivity of the numerical simulation to the grid size and time step was investigated to ensure that the right mesh and time step has been chosen. Figure 2b and c shows the maximum wall shear stress, i.e., one of the most sensitive parameters in relation to grid size, during the time for different grid sizes (course, medium, and fine) and time steps (12.5, 25, and 50 ns). As evident from these graphs, the variation of the simulation results was within an acceptable range. Therefore, the medium mesh and time step of 25 ns was chosen for follow-up simulations and analysis.

3.3. Transition from a droplet to a jet

Figure 3 depicts the geometrical parameters used to describe the dispensing dynamics of a droplet, and
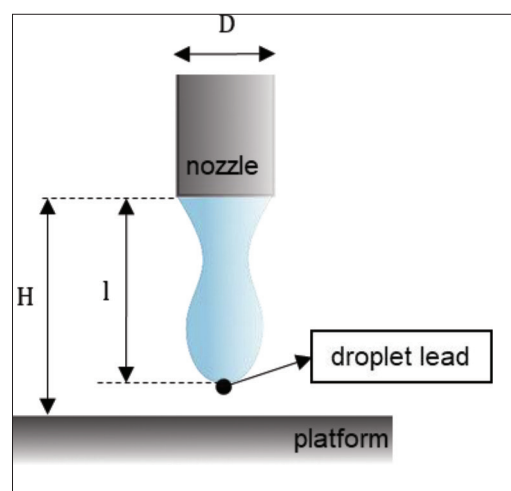
Figure 3. The geometrical parameters used to describe the dispensing process. H, l, and D indicate nozzle-to-platform distance, droplet lead vertical position, and nozzle diameter, respectively.

Figure 4 illustrates the dispensing dynamics predicted by simulation model considering two nozzle sizes, 150 μm and 300 μm, at different upstream hydrostatic pressures. Alginate 1.5% w/v and air at 25°C were considered the liquid and gas phases, respectively. The nozzle-to-platform distance (H) was set to 1.2 mm for both microvalves. At low upstream pressure, i.e., 0.8 bar for the 150-μm nozzle

and 0.3 bar for the 300-μm nozzle, no droplet was formed (first row in Figure 4a and b, respectively). As the upstream pressure was slightly increased, a single droplet was formed, pinched-off, and impinged on the platform (second and third rows in Figure 4a and b). Increasing the upstream pressure resulted in formation of a ligament following the main droplet that impinged on the platform (fourth row in Figure 4a and b). At relatively higher upstream pressure, a larger ligament formed a jet between the nozzle and platform that eventually pinched-off (fifth row in Figure 4a and b). The ligament pinch-off time was mainly affected by nozzle size but slightly also by upstream pressure (Table 2). In the case of the 150-μm nozzle, the ligament pinched-off between 750 and 930 μs, while for the 300-μm nozzle, the ligament pinched-off between 1660 and 1720 μs. In the case of the piezoelectric microvalve, a droplet pinch-off in less than 400 μs has been reported[14,15,27].

The average alginate velocity at the outlet of the nozzle is depicted versus time in Figure 4c and d for both nozzle sizes. Obviously, the average velocity increases by time at the beginning and drops suddenly to zero at $t = 400$ μs, i.e., when the microvalve closes. While the flow inside the nozzle reached a steady state after about 150 μs for the small nozzle size, it was transient throughout the entire opening time for the bigger nozzle. The one-dimensional solution of a quasi-steady laminar flow in a circular pipe is given by

$$v(t) = \frac{\Delta P D^2}{32 \mu L}\left(1 - e^{-\frac{32\mu}{\rho D^2}t}\right) \qquad (III)$$

Based on Equation III, the characteristic time for reaching a steady-state condition is proportional to $\rho D^2/32\mu$, i.e., the bigger the nozzle size, the longer it takes to reach a steady-state condition independent of pressure difference amplitude. Our results were consistent with this theory.

Figures 3f and 4e show the leading point vertical position of the droplet versus time at different upstream pressure for 150-μm and 300-μm microvalves, respectively. Here, the droplet leading position (l) can vary between 0 (at the nozzle tip) and 1.2 mm (when the tip of the droplet touches the platform at a vertical position of 1.2 mm with respect to the nozzle). For very low upstream pressure, the driving force within the fluid is insufficient to overcome the surface tension and form a droplet (beige color in the graphs). The process of droplet formation and pinch-off is described by Reynolds Reynolds ($Re = \rho v d/\mu$), Weber ($We = \rho v^2 d/\sigma$), and Ohnesorge ($Oh = \sqrt{We}/Re$) numbers[12-15,27]. The respective values of these dimensionless parameters calculated based on the average alginate velocity at the outlet and at $t = 400$ μs for each case are reported in Table 2. In this table, the minimum

Re and maximum Oh correspond to those calculated with zero shear viscosity. By increasing the upstream pressure, Re and We increase, while the Oh remains constant and independent of upstream pressure.

The speed of droplet lead point was calculated based on second-order centered finite difference formula (Equation IV). The results are depicted in Figure 4g and h for 150 and 300 μm microvalves, respectively, for different upstream pressures. In all cases, the speed of the lead point of the droplet was lower than the average alginate velocity at the outlet of the nozzle. These differences became more evident for the larger nozzle and as the transition from droplet to jet occurred.

$$v_{droplet}(t) = \frac{x_{lead}(t + \Delta t) - x_{lead}(t - \Delta t)}{2\Delta t} + O(\Delta t^2) \qquad (IV)$$

Another interesting observation was the fluctuation in droplet speed while traveling the distance between nozzle and platform. This has also been reported during droplet ejection using piezoelectric microvalves for 1–2% w/v alginate solutions[15]. The We calculated by the maximum droplet lead-point speed was compared with the We calculated by average alginate velocity at the outlet of the nozzle and presented in Figures 4b and 5a for 150 and 300 μm microvalves, respectively. In general, larger nozzle size leads to a higher We number due to an increase in inertia with respect to surface tension. For the bigger nozzle, as the upstream pressure was increased, the difference between the two numbers was magnified. This is explained by the observation that as the transition from droplet to jet occurred, a bigger difference between droplet speed and average alginate velocity at the outlet of nozzle occurred.

3.4. Impingement shear stress and nozzle wall shear stress

The maximum wall shear stress in the nozzle increased during the opening time of the microvalves and reached a maximum level precisely before microvalve closure (Figure 6a and b; **Figure S1** in Supplementary File). After that point, wall shear stress inside the nozzle decreased suddenly and remained at a very low level (because of ligament retraction effect) until the end of the dispensing process. The magnitude of the maximum wall shear stress inside the nozzle increased with upstream pressure in a semi-linear fashion. The spatial distribution of wall shear stress inside the nozzle for the case of D = 300 μm and P = 1.0 bar is presented as a contour plot in **Figure S1a** (Supplementary File) at four selected time points of 200, 300, 400, and 500 μs after opening of the nozzle. The maximum of nozzle wall shear stress occurs at the inlet of the nozzle.

During the impinging, the kinetic energy of the droplet dissipates through deformation and friction force
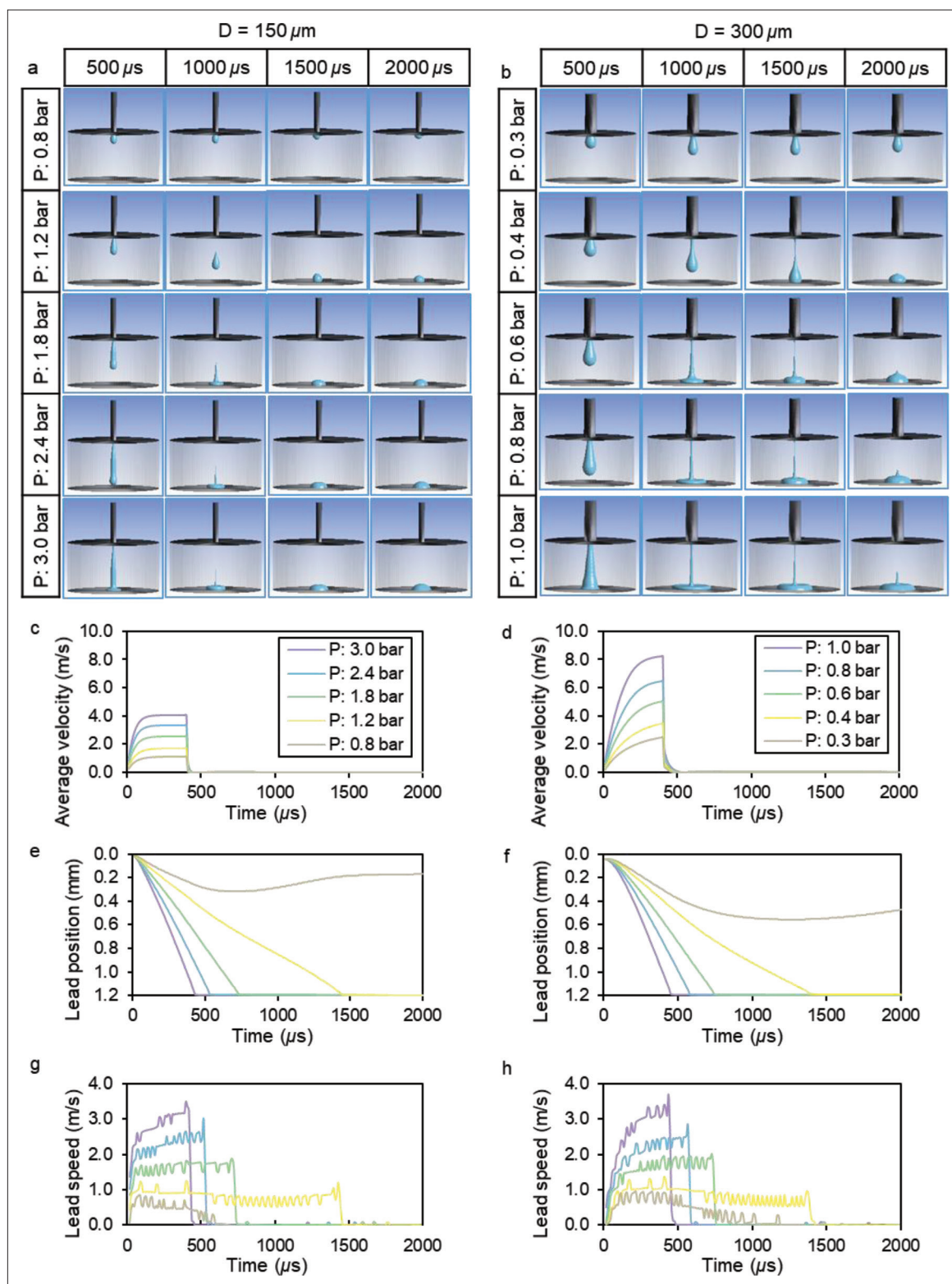
Figure 4. Microvalve dispensing dynamics. A transition from droplet to jet formation was observed when upstream pressure was increased: snapshots of dispensed alginate at four time points (t = 500, 1000, 1500, and 2000 μs) after nozzle opening for nozzle diameters of 150 μm (a) and 300 μm (b) at different upstream pressure are presented. Average alginate velocity at the outlet of the nozzle is plotted versus time for (c) nozzle diameter of 150 μm and (d) 300 μm. The position of the lead point of the droplet is plotted versus time for (e) nozzle diameter of 150 μm and (f) 300 μm. The speed of droplet lead point was calculated using Equation IV and plotted for (g) nozzle diameters of 150 μm and (h) 300 μm.

Table 2. Ligament pinch-off time, Reynolds, Weber, and Ohnesorge numbers at different upstream pressures for both nozzle sizes

|	D = 150 μm					
P (Pa)	Pinch-off time (μs)	Re_{max}	Re_{min}	We	Oh_{max}	Oh_{min}
0.8	No pinch-off	5.56	0.53	3.72	3.64	0.35
1.2	920–930	8.56	0.81	8.80	3.64	0.35
1.8	820–830	12.73	1.21	19.47	3.64	0.35
2.4	790–800	16.66	1.59	33.34	3.64	0.35
3.0	750–760	20.40	1.94	50.01	3.64	0.35
	D = 300 μm					
P (Pa)	Pinch-off time (μs)	Re_{max}	Re_{min}	We	Oh_{max}	Oh_{min}
0.3	No pinch-off	25.04	2.38	37.65	2.57	0.25
0.4	1700–1710	34.45	3.28	71.29	2.57	0.25
0.6	1660–1670	50.71	4.83	154.44	2.57	0.25
0.8	1660–1670	64.52	6.14	250.02	2.57	0.25
1.0	1710–1720	82.49	7.86	408.68	2.57	0.25

The pinch-off time represents the time when the ligament detached from the nozzle. The dimensionless parameters were calculated based on the alginate average velocity at the outlet of nozzle at $t = 400$ μs.. The zero shear viscosity of 0.315 Pa·s and infinite shear viscosity of 0.03 Pa·s and a surface tension of 0.05 N·m^{-1} were used.

inside the alginate and between alginate and platform until a stationary droplet stabilizes on the platform. The spatial distribution of impingement shear stress on the platform for the case of D = 300 μm and P = 1.0 bar is presented as a contour plot in **Figure S1a** (Supplementary File) at three selected time points of 460, 500, and 600 μs after opening of the nozzle. The contour plot shows that the maximum of impingement shear stress occurs at the proximity of the stagnation point at the beginning of impingement. In **Figure S1b** (Supplementary File), the dispensing dynamics captured by high-speed camera and resulting from the simulation are plotted together with nozzle and impingement wall shear stress during 2000 μs. Figure 6c and d shows the maximum shear stress on the platform versus time for 150-μm and 300-μm nozzles, respectively. As is shown, for each of the upstream pressures at first, the shear stress on the platform was zero, which then increased suddenly to a maximum level (when the droplet impinged on the platform), and then, it decreased over time as the droplet was spreading on the platform surface. The impingement shear stress increased by pressure in a non-linear fashion. Surprisingly, the ratio between the maximum shear stress on the platform and the maximum wall shear stress in the nozzle increased by upstream pressure (Figure 6e and f). This indicates
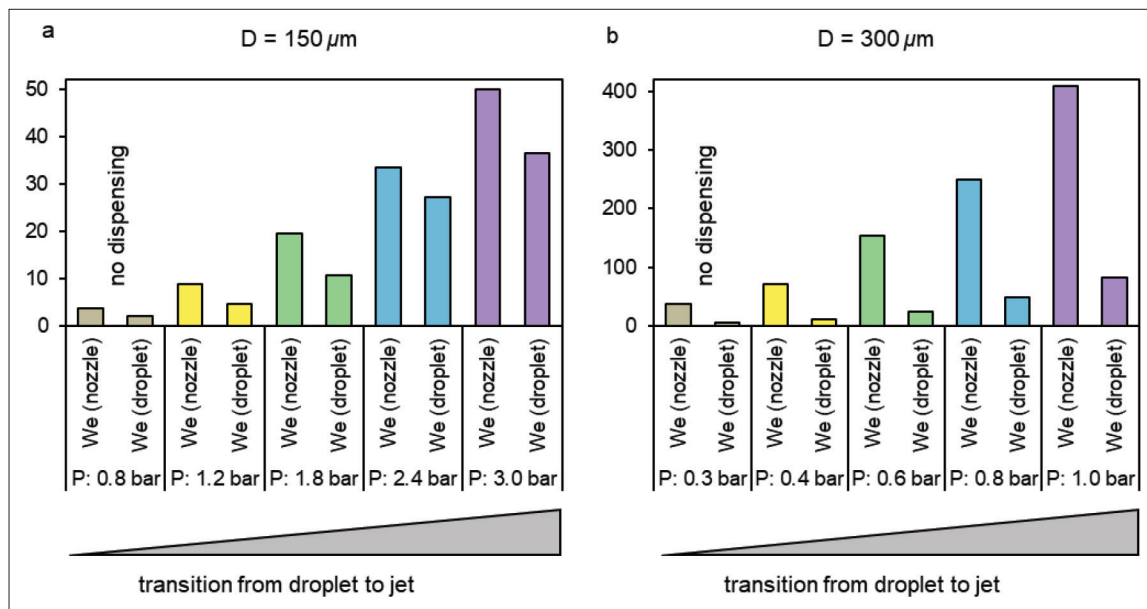
Figure 5. Weber number calculated by average alginate velocity at the outlet of nozzle in comparison to that calculated by droplet lead-point speed for (a) 150-μm and (b) 300-μm microvalves at different upstream pressure. The *We* increases with increasing hydrostatic pressure. As upstream pressure increases, the difference between the two calculated numbers is magnified.
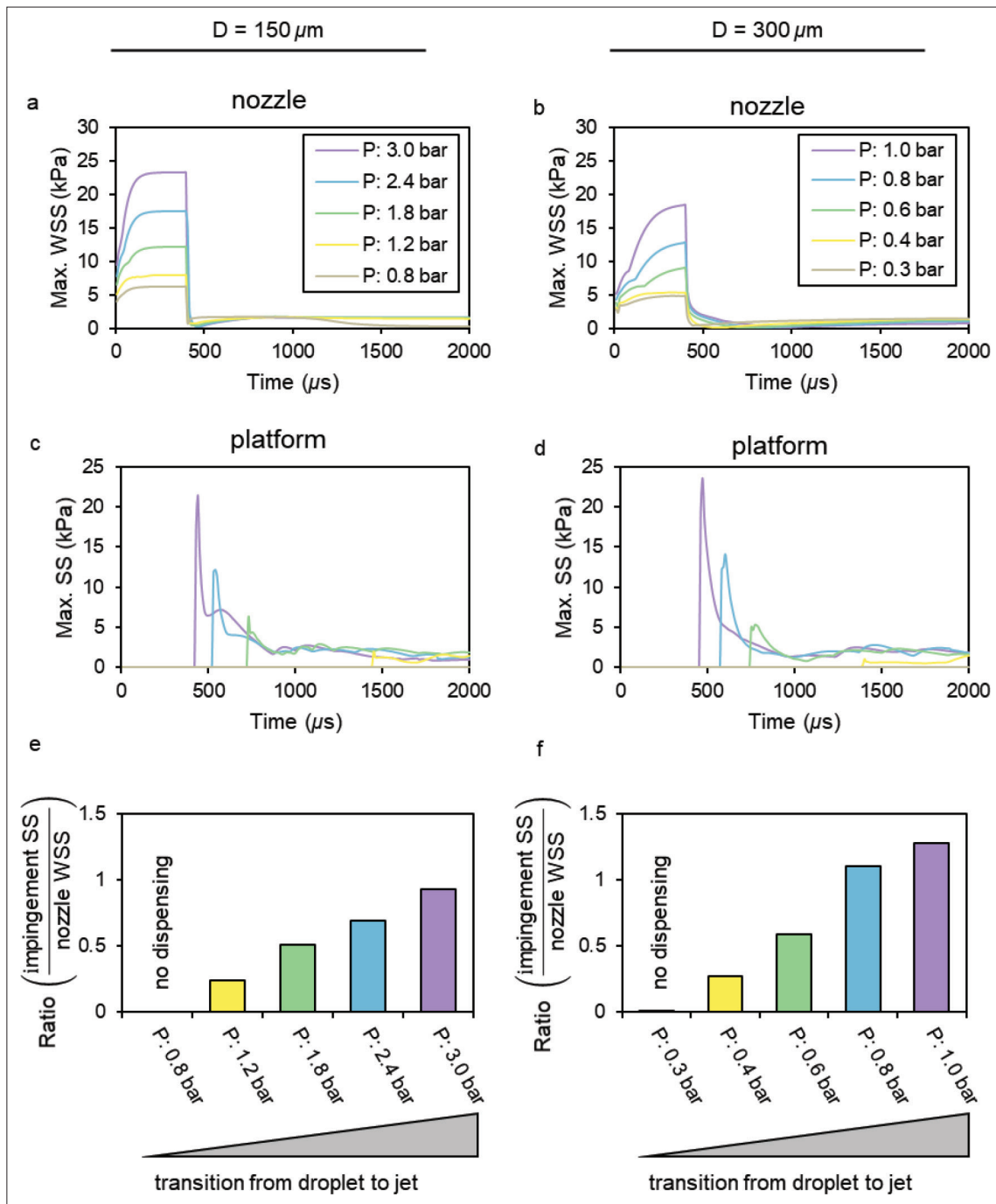
Figure 6. Nozzle maximum wall shear stress (WSS) versus impingement maximum shear stress (SS) during dispensing. A transient increase in maximum wall shear stress in the nozzle was observed for both nozzle sizes, (a) 150 μm and (b) 300 μm. The maximum wall shear stress increased by pressure in an almost linear fashion for both nozzle sizes. The impingement maximum shear stress is plotted versus time for different upstream pressure for both nozzle sizes in (c) and (d). The impingement shear stress increases in a non-linear fashion with upstream pressure. The ratio of the impingement shear stress on the platform to the nozzle wall shear stress is depicted in (e) and (f) for both nozzles. As the flow regime transition from droplet to jet occurs, the impingement shear stress becomes dominant.
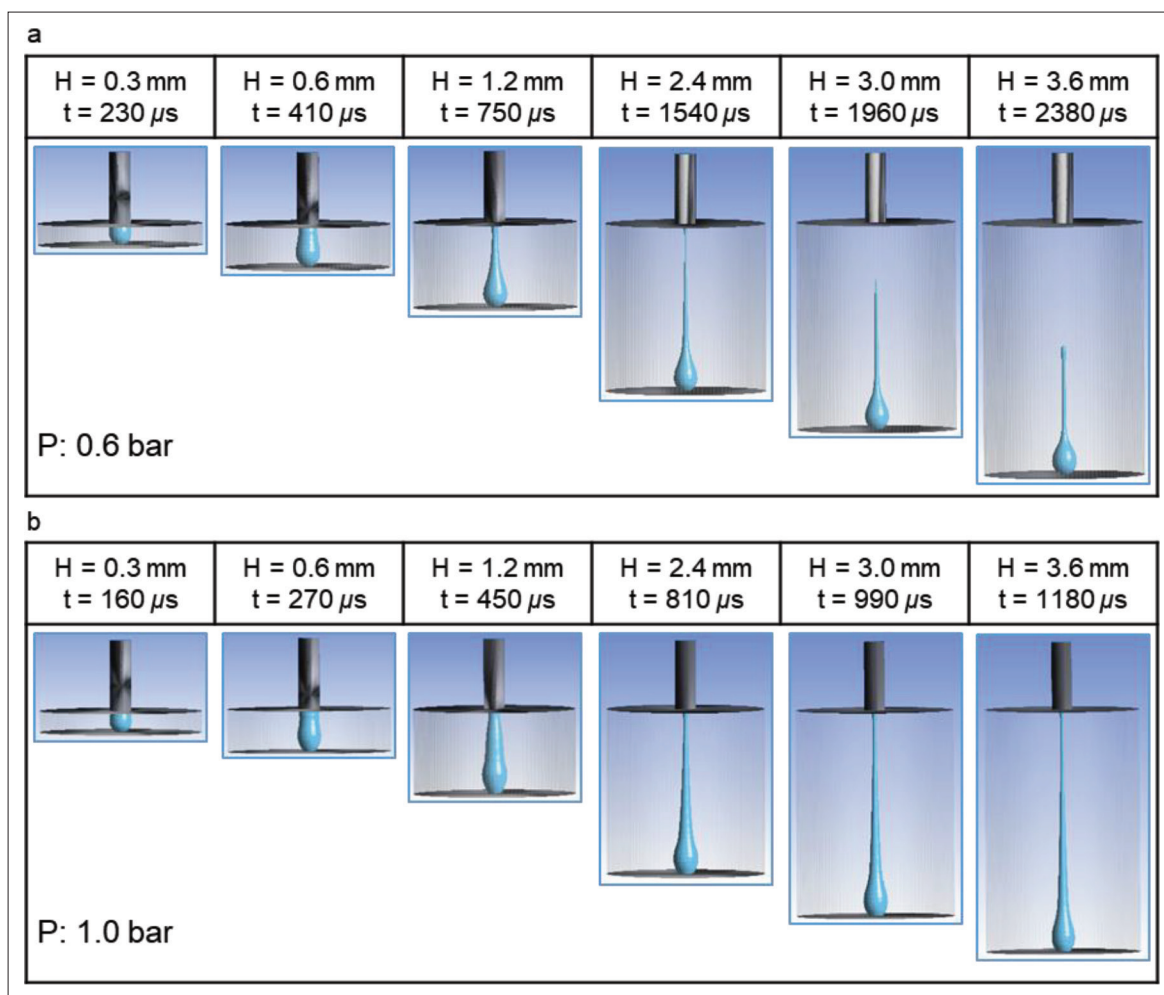
Figure 7. Simulated droplet formation when it touches the building platform at different distances (H) between nozzle tip and platform, for upstream pressure of (a) 0.6 bar and (b) 1.0 bar. The nozzle size was 300 μm in both simulations.

that at low upstream pressure, i.e., when a droplet with a small ligament is forming, nozzle wall shear stress is dominant (wall shear stresses ratio less than 1.0), while at higher upstream pressure, i.e., when a jet is forming, the platform shear stress exceeds the nozzle wall shear stress and becomes dominant (wall shear stresses ratio more than 1.0). The rate of increase of wall shear stress ratio as a function of upstream pressure was higher for the bigger nozzle size, i.e., a linear functional fit to the data revealed a slope of 1.87 (R^2 = 0.98) for 300-μm nozzle and a slope of 0.43 (R^2 = 0.97) for 150-μm nozzle (not presented in the graphs).

3.5. Effect of nozzle-to-platform distance (H) on impingement shear stress

The simulation model was used to determine whether nozzle-to-platform distance plays a role in the ratio of impingement shear stress to nozzle wall shear stress

(Figures 7 and 8). Figure 7a and b presents a snapshot of the moment that the droplet/jet lead point touches the platform at various H and for upstream pressure of 0.6 and 1.0 bar, respectively. Considering the nozzle size of 300 μm, as H increased, the nozzle wall shear stress remained constant independent of H for two sample upstream pressures of 0.6 bar (Figure 8a) and 1.0 bar (Figure 8b). However, the impingement shear stress changed if H varied (Figure 8c and d). At low upstream pressure, increasing H from 0.3 to 3.6 mm resulted in a variation of impingement shear stress between 3.73 and 6.01 kPa with maximum stress occurring at H = 0.6 mm. At high upstream pressure, the same change in H resulted in variation of impingement maximum shear stress of between 12.57 and 27.01 kPa, with its maximum predicted at H = 2.4 mm. The ratio of impingement shear stress to the nozzle wall shear stress for both cases is plotted in Figure 8e and f, demonstrating that regardless of the nozzle-to-platform distance, at low upstream pressure
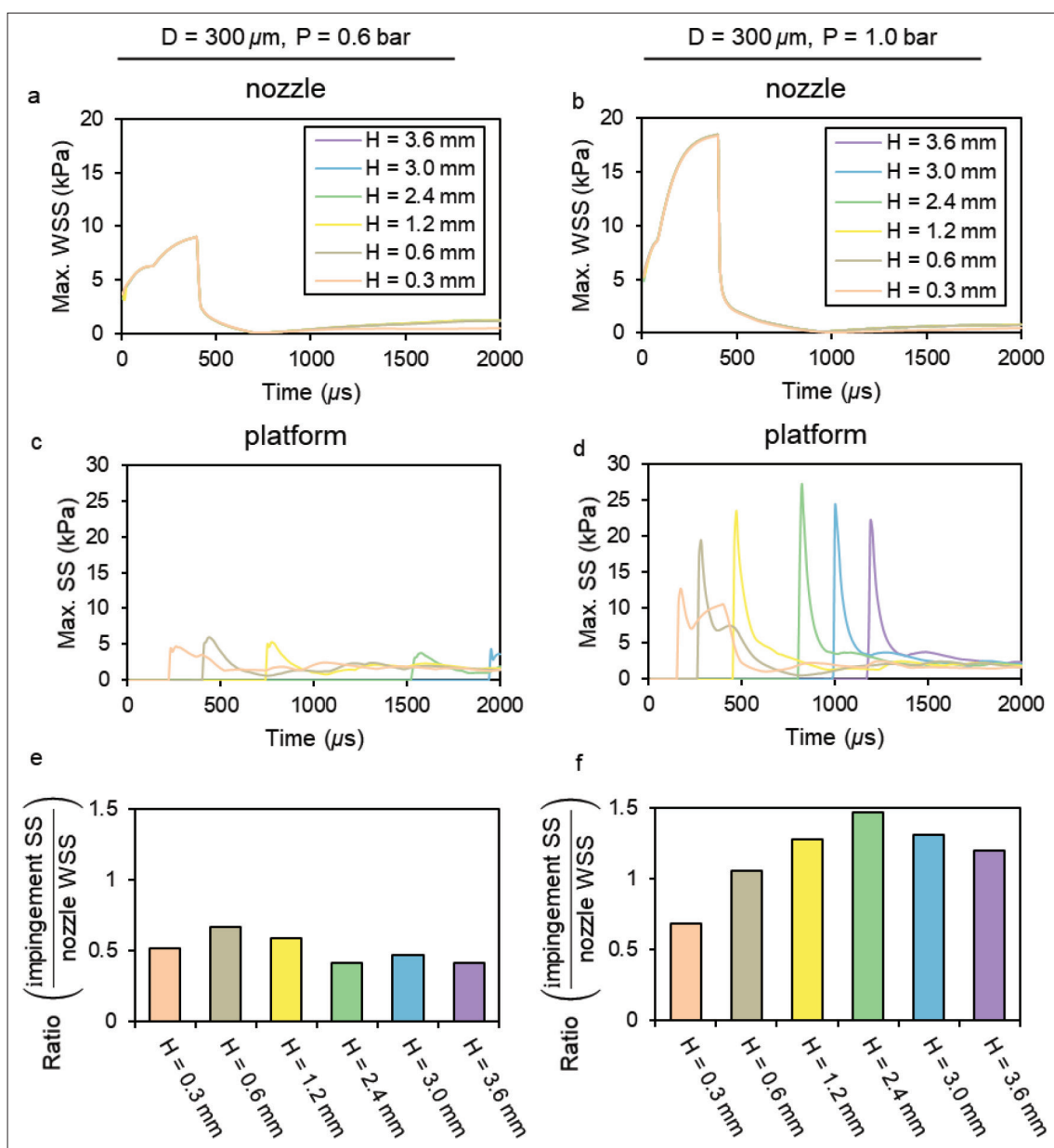
Figure 8. Nozzle wall shear stress (WSS) and impingement shear stress (SS) as a function of nozzle-to-platform distance (H). Maximum wall shear stress inside the nozzle remained constant regardless of H for both upstream pressures at (a) 0.6 bar and (b) 1.0 bar. Impingement maximum shear stress varied as a function of H for both upstream pressures at (c) 0.6 bar and (d) 1.0 bar. The ratio of the impingement shear stress to nozzle wall shear stress varied as a function of H for both upstream pressures at (e) 0.6 bar and (f) 1.0 bar. Impingement shear stress was dominant with high variation for H in the case of 1.0 bar upstream pressure. In (c), the data for H = 36 are not presented because the droplet impingement occurred after 2000 μs, which is outside of the time window of all presented simulation data.

(i.e., when a droplet is forming), nozzle wall shear stress is dominant. However, at relatively higher upstream pressure (i.e., when jet is forming), the impingement shear stress is almost dominant with a higher rate of variation with regard to H.

To validate the numerical simulations, a series of *in vitro* experiments were performed. A microvalve with

nozzle size of 300 μm was placed at different vertical distances (0.3, 0.6, 1.2, 2.4, and 3.0 mm) from the platform, and droplet of cell-suspended alginate solution was dispensed at two different upstream pressures of 0.6 and 1.0 bar. By changing the nozzle-to-platform distance at constant upstream pressure, the impingement shear stress varies while the nozzle wall shear stress remains constant. Figure 9a presents the sample fluorescent images
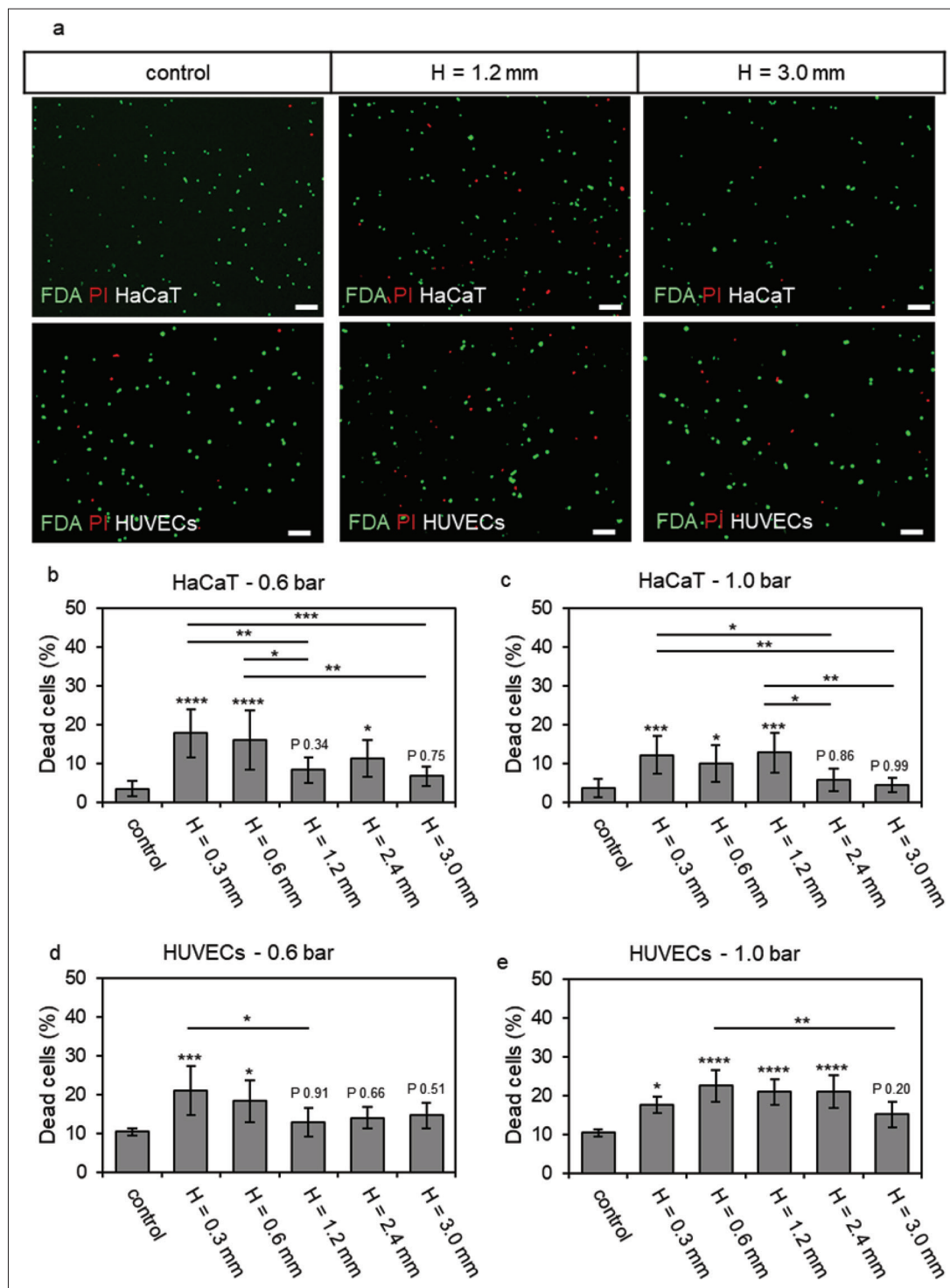
Figure 9. Cell death due to impingement shear stress. (a) Sample fluorescent images of the cell-suspension alginate solution, stained with fluorescein diacetate (FDA) and propidium iodide (PI), after dispensing from nozzle at upstream pressure of 1.0 bar for nozzle-to-platform distance of H = 1.2 mm and 3.0 mm, respectively. "Control" corresponds to cells from the reservoir of the microvalve that did not experience nozzle and impingement shear stress. A greater number of dead cells (red signal) were detected at H lower than 1.2 mm for HaCaT (b) and HUVECs (d) at upstream pressure of 0.6 bar. At 1.0 bar upstream pressure, a large number of dead cells were detected for H lower than 3.0 mm for HaCaT (c) and HUVECs (e). The values are presented as mean ± standard deviation (SD). $n \geq 3$, $*p < 0.05$, $**p < 0.01$, $***p < 0.001$, and $****p < 0.0001$. The scale bars in the micrographs represent 75 µm.

of the cell-suspension alginate solution stained with FDA and PI after dispensing from the nozzle at upstream pressure of 1.0 bar for two nozzle-to-platform distances of 1.2 and 3.0 mm. The "control" corresponds to the cells' uptake from the nozzle without experiencing nozzle and impingement shear stress. The images show that a higher number of dead cells are visible when the nozzle is at a 1.2-mm distance from the platform for both HaCaT cells and HUVECs. The same experiment was then performed at different distances (H). The percentage of dead cells was measured for HaCaT (Figure 9b and c) and HUVECs (Figure 9d and e) at upstream pressures of 0.6 and 1.0 bar, respectively. Viability investigation of the cells dispensed at upstream pressure of 0.6 bar revealed that at a distance below 1.2 mm from the platform, a highly statistically significant number of cells died due to impingement shear stress. However, at a greater distance (H), the observed reduction in viability rate did not reach statistical significance. Overall, the optimum distance from the platform for 1.0 bar upstream pressure was 2.4 and 3.0 mm for HaCaT cells and HUVECs, respectively.

4. Discussion

Increasing the printing resolution during nozzle-based bioprinting leads to harsh mechanical conditions inside the nozzle, causing cell death and limiting printing speed. Because of this, extrusion bioprinting can be categorized as a slow bioprinting method with the most negative effects on cell viability, mainly due to long nozzle length and high wall shear stress. In order to increase the printing speed and resolution while decreasing process-induced cell death, droplet-based printing techniques were developed[28]. Droplet-based techniques, such as drop-on-demand, usually require the use of low viscous bioinks in the range lower than 30 mPa·s[2,29,30]. However, bioinks with relatively higher viscosity can still be printed using solenoid microvalves.

In this work, considering the minimum opening time of the microvalve (400 µs as recommended by the manufacturer [Fritz Gyger AG, Gwatt, Switzerland]) and using the simulation model, we explored how dispensing dynamics are affected by changing the upstream pressure for two different nozzle sizes commonly used in bioprinting[20,31]. Three dispensing dynamics were observed. At low upstream pressure, the kinetic energy was insufficient for the droplet to overcome the interfacial force and pinch-off. As a result, a droplet formed but remained attached to the tip of the nozzle. At mid upstream pressure, droplet and ligament were dispensed and eventually pinched-off. At high upstream pressure, a jet of alginate solution was dispensed from the nozzle and impinged on the platform.

There are a number of studies focusing on the dynamics of drop ejection during printing using piezoelectric microvalves that categorize printable and non-printable inks/bioinks. For example, the conditions for ink/bioink to be printable have been discussed as in [12]: $1 < 1/Oh < 10$ and $We > 4$ or in [13,27]: $4 < 1/Oh < 14$ and $We > 4$. Therefore, a certain range of concentration can usually be identified within which specific bioinks can be printed using certain nozzle sizes[13]. Generalization of those studies to the use of solenoid microvalves remains questionable because solenoid and piezoelectric microvalves differ in their actuation principles. For example, in our study, no droplet was formed at a Weber number of 37.65 when using a 300 µm microvalve (corresponding to Weber number of 5.37 based on droplet speed). The time required for the droplet ligament to pinch-off was 800 and 1700 µs for small and large nozzles, respectively, while a pinch-off time of about 200–400 µs, probably due to smaller nozzle size, was reported for 1%–2% alginate solutions using piezoelectric microvalves[15]. Regarding the pinch-off position, however, similar to them, an exit/middle pinch-off location was predicted in our simulation. Furthermore, Xu et al.[15] discussed how during the droplet formation of a viscoelastic fluid the process is governed by the inertial, viscous, elastic, and capillary effects. The ligament formation and its length are mainly governed by the balance among these effects, while the gravitational effect can be ignored due to the small Bond number.

When the bioink properties and microvalve physical parameters such as nozzle size and opening time are suitable for stable droplet ejection, further increasing upstream pressure results in a higher dispensing flow rate, which leads to a bigger droplet or a droplet with a larger ligament. If the ligament size is bigger than the nozzle-to-platform distance, a jet forms between the nozzle and platform for a short period during dispensing. As a consequence of higher flow rate, the nozzle wall shear stress also increases. In a bioprinting scenario, it has been shown that the nozzle wall shear stress is a limiting factor as it can directly rupture the cell membrane[25]. However, here we show that the impingement shear stress is at a level comparable to nozzle wall shear stress and, in some cases, even exceeds it. Therefore, during solenoid microvalve bioprinting, the impingement shear stress is an additional parameter needed to be minimized for reducing process-induced cell death. It was observed that at relatively low upstream pressure, the nozzle wall shear stress is the dominant deteriorating factor, while at relatively high upstream pressure, impingement shear stress is the factor/parameter most affecting the cell viability. Furthermore, at high upstream pressure, the impingement shear stress strongly depends upon nozzle-to-platform distance. The

maximum impingement shear stress was at H = 2.8 mm. Phares et al.[32] also reported an analytical relation to calculate the maximum wall shear stress in axisymmetric fully developed steady-state jet impingement as:

$$\tau_{max.} = 44.6\rho v^2\, \text{Re}^{-\frac{1}{2}} \left(\frac{H}{D}\right)^{-2}, \quad \frac{H}{D} < 8 \tag{V-a}$$

$$\tau_{max.} = 0.70\rho v^2\, \text{Re}^{-\frac{1}{2}}, \quad \frac{H}{D} < 8 \tag{V-b}$$

The above formula shows that the maximum impingement shear stress occurs at H / D = 8, which matches our results at high upstream pressure. However, it was not confirmed at low upstream pressure when a droplet was forming. In another study, Yonemoto and Kunugi[33] used an analytical approach based on an integral method and energy conservation to characterize the impingement of a spherical droplet on solid surfaces. They defined two regions: In capillary regions, the viscous dissipation is negligible. Therefore, during impingement, the kinetic energy of a droplet converts to adhesion and deformation energies. In the viscous region, the kinetic energy of a droplet mainly dissipates through the viscous dissipation. After some mathematical procedures and simplification, they showed that the total viscous dissipation energy during droplet imping for a Newtonian fluid can be calculated as:

$$E_{vis.} = \frac{81}{64}\frac{\mu r_m}{h_m^2} u_d Q \tag{VI}$$

Where u_d, r_m, μ, and Q are droplet speed (m/s), droplet maximum spreading radius (m), liquid viscosity (Pa·s), and droplet volume (m³), respectively, and h_m is calculated as a function of dimensionless maximum spreading diameter during imping. Since Equation VI is obtained based on an integral method, it offers an approximation of average energy dissipation by shear and extensional stress through the entire droplet spreading. A simple conclusion from the above equation is that the dissipation energy (and consequently the shear and extensional stress) increases by droplet velocity and volume. This is consistent with our numerical results as we captured higher impingement shear stress by increasing either nozzle size or upstream pressure. Nevertheless, even if some agreement was observed between our simulation results and the mentioned studies, the fully developed and steady-state assumptions (in deriving Equation V), fully spherical droplet (in deriving Equation VI), and Newtonian fluid assumption (in both equations) are not valid during droplet ejection of cell-suspended alginate solution using a solenoid microvalve. Additionally, a valuable future prospect would be to evaluate whether the bioink surface tension can be used to modulate the impingement shear stress.

To validate the results of numerical simulation and our hypothesis that the impingement shear stress has a detrimental effect on cell survival during microvalve bioprinting, we conducted a simple experiment: We printed cell suspension of alginate solution at constant upstream pressure but at different H. At low upstream pressure (0.6 bar), when the nozzle was very close to the platform (H < 1.2 mm and D = 300 μm), a significant number of cells were dead regardless of type (HaCaT and HUVECs). At higher upstream pressure (1.0 bar), a significant number of dead cells was observed for H < 2.4 mm for both cell types. Since the nozzle wall shear stress is independent of H, the cell death at lower H can be attributed to impingement shear stress. Therefore, depending on upstream pressure, a minimum distance between the nozzle and platform is required to optimize the cell viability during microvalve bioprinting. In a real three-dimensional (3D) bioprinting scenario, the biological structure is built layer-by-layer[34,35]. We believe that the results presented here are still valid for such cases because the viability assessments have been performed for ten drops of hydrogel printed on top of each other.

The simulation predicted lower impingement shear stress at a very short distance between nozzle and platform. However, the viability assessment did not confirm significant cell viability impediment at short distances (low H). This discrepancy might be due either to experimental deviation at short distances between nozzle and platform or to idealized hydrogel properties set in the simulation.

5. Conclusion

In this work, we used a numerical simulation model of droplet ejection during microvalve-based bioprinting to calculate impingement and nozzle wall shear stress. For bioink, the physical properties of alginate 1.5% w/v were used. The numerical results, validated by experimental evaluations, revealed that the impingement-related shear stress can exceed the wall shear stress in the nozzle in microvalve-based bioprinting. The amplitude of impingement shear stress depended on nozzle-to-platform distance. Therefore, this critical issue should be addressed by the adjustment of the distance between the nozzle and the building platform to optimize the cell viability.

Acknowledgments

Funding

Conflict of interest

The authors declare no conflict of interest.

Author contributions

Conceptualization: Ramin Nasehi, Horst Fischer
Formal analysis: Ramin Nasehi
Investigation: Ramin Nasehi
Methodology: Ramin Nasehi
Writing – original draft: Ramin Nasehi
Writing – review & editing: Ramin Nasehi, Sanja Aveic, Horst Fischer

Ethics approval and consent to participate

Primary HUVECs were isolated from umbilical cords provided by the Department of Gynecology and Perinatal Medicine, RWTH Aachen University Hospital, Aachen, Germany, as approved by the local ethics committee of the Faculty of Medicine at RWTH Aachen University (EK 424/19).

Consent for publication

Not applicable.

Availability of data

Research data are available from the authors on request.

Further disclosure

Not applicable.

References

1. Noor N, Shapira A, Edri R, *et al.,* 2019, 3D printing of personalized thick and perfusable cardiac patches and hearts. *Adv Sci,* 6(11): 1900344.

2. Li X, Liu B, Pei B, *et al.,* 2020, Inkjet bioprinting of biomaterials. *Chem Rev,* 120(19): 10793–10833.

3. Ng WL, Lee JM, Yeong WY, *et al.,* 2017, Microvalve-based bioprinting – process, bio-inks and applications. *Biomater Sci,* 5(4): 632–647.

4. Ng WL, Lee JM, Zhou M, *et al.,* 2020, Vat polymerization-based bioprinting—process, materials, applications and regulatory challenges. *Biofabrication,* 12(2): 022001.

5. Ebrahimi Orimi H, Hosseini Kolkooh SS, Hooker E, *et al.*, 2020, Drop-on-demand cell bioprinting via laser induced side transfer (LIST). *Sci Rep,* 10(1): 9730.

6. Keriquel V, Oliveira H, Rémy M, *et al.*, 2017, In situ printing of mesenchymal stromal cells, by laser-assisted bioprinting, for in vivo bone regeneration applications. *Sci Rep,* 7(1): 1778.

7. Jentsch S, Nasehi R, Kuckelkorn C, *et al.,* 2021, Multiscale 3D bioprinting by nozzle-free acoustic droplet ejection. *Small Methods,* 5(6): e2000971.

8. Shafiee A, Ghadiri E, Ramesh H, *et al.,* 2019, Physics of bioprinting. *Appl Phys Rev,* 6(2): 021315.

9. Gudapati H, Dey M, Ozbolat I, 2016, A comprehensive review on droplet-based bioprinting: Past, present and future. *Biomaterials,* 102: 20–42.

10. Raees S, Ullah F, Javed F, *et al.*, 2023, Classification, processing, and applications of bioink and 3D bioprinting: A detailed review. *Int J Biol Macromol,* 232: 123476.

11. Lee JM, Sing SL, Zhou M, *et al.,* 2018, 3D bioprinting processes: A perspective on classification and terminology. *Int J Bioprint,* 4(2): 151.

12. Derby B, 2010, Inkjet printing of functional and structural materials: Fluid property requirements, feature stability, and resolution. *Annu Rev Mater Res,* 40(1): 395–414.

13. Gudapati H, Parisi D, Colby RH, *et al.,* 2020, Rheological investigation of collagen, fibrinogen, and thrombin solutions for drop-on-demand 3D bioprinting. *Soft Matter,* 16(46): 10506–10517.

14. Gudapati H, Ozbolat IT, 2020, The role of concentration on drop formation and breakup of collagen, fibrinogen, and thrombin solutions during inkjet bioprinting. *Langmuir,* 36(50): 15373–15385.

15. Xu C, Zhang Z, Fu J, *et al.,* 2017, Study of pinch-off locations during drop-on-demand inkjet printing of viscoelastic alginate solutions. *Langmuir,* 33(20): 5037–5045.

16. Chand R, Shimwa Muhire B, Vijayavenkataraman S, 2022, Computational fluid dynamics assessment of the effect of bioprinting parameters in extrusion bioprinting. *Int J Bioprint,* 8(2): 545.

17. Emmermacher J, Spura D, Cziommer J, *et al.*, 2020, Engineering considerations on extrusion-based bioprinting: Interactions of material behavior, mechanical forces and cells in the printing needle. *Biofabrication,* 12(2): 25022.

18. Ng WL, Huang X, Shkolnikov V, *et al.*, 2021, Controlling droplet impact velocity and droplet volume: Key factors to achieving high cell viability in sub-nanoliter droplet-based bioprinting. *Int J Bioprint,* 8(1): 424.

19. Xu H, Liu Q, Casillas J, *et al.,* 2022, Prediction of cell viability in dynamic optical projection stereolithography-based bioprinting using machine learning. *J Intell Manuf,* 33(4): 995–1005.

20. Blaeser A, Duarte Campos DF, Puster U, *et al.*, 2016, Controlling shear stress in 3D bioprinting is a key factor to balance printing resolution and stem cell integrity. *Adv Healthc Mater,* 5(3): 326–333.

21. Köpf M, Nasehi R, Kreimendahl F, *et al.,* 2022, Bioprinting-associated shear stress and hydrostatic pressure affect the angiogenic potential of human umbilical vein endothelial cells. *Int J Bioprint,* 8(4): 96–107.

22. Ning L, Betancourt N, Schreyer DJ, *et al.*, 2018, Characterization of cell damage and proliferative ability during and after bioprinting. *ACS Biomater Sci Eng*, 4(11): 3906–3918.

23. Guillemot F, Souquet A, Catros S, *et al.*, 2010, Laser-assisted cell printing: Principle, physical parameters versus cell fate and perspectives in tissue engineering. *Nanomedicine,* 5(1): 507–515.

24. Ringeisen BR, Kim H, Barron JA, *et al.,* 2004, Laser printing of pluripotent embryonal carcinoma cells. *Tissue Eng,* 10(3-4): 483–491.

25. Paxton N, Smolan W, Böck T, *et al.,* 2017, Proposal to assess printability of bioinks for extrusion-based bioprinting and evaluation of rheological properties governing bioprintability. *Biofabrication,* 9(4): 044107.

26. Boukamp P, Petrussevska RT, Breitkreutz D, *et al.*, 1988, Normal keratinization in a spontaneously immortalized aneuploid human keratinocyte cell line. *J Cell Biol,* 106(3): 761–771.

27. Jang D, Kim D, Moon J, 2009, Influence of fluid physical properties on ink-jet printability. *Langmuir,* 25(5): 2629–2635.

28. Ravanbakhsh H, Karamzadeh V, Bao G, *et al.*, 2021, Emerging technologies in multi-material bioprinting. *Adv Mater,* 33(5):2104730.

29. Derby B, Reis N, 2003, Inkjet printing of highly loaded particulate suspensions. *MRS Bull,* 28(11): 815–818.

30. Saunders RE, Derby B, 2014, Inkjet printing biomaterials for tissue engineering: Bioprinting. *Int Mater Rev,* 59(8): 430–448.

31. Duarte Campos DF, Blaeser A, 2021, 3D-bioprinting, in Kasper C, Egger D, Lavrentieva A (eds), *Basic Concepts on 3D Cell Culture. Learning Materials in Biosciences,* Springer, Cham.

    https://doi.org/10.1007/978-3-030-66749-8_9

32. Phares DJ, Smedley GT, Flagan RC, 2000, The wall shear stress produced by the normal impingement of a jet on a flat surface. *J Fluid Mech,* 418: 351–375.

33. Yonemoto Y, Kunugi T, 2017, Analytical consideration of liquid droplet impingement on solid surfaces. *Sci Rep,* 7(1): 2362.

34. AlZaid S, Hammad N, Albalawi HI, *et al.,* 2022, Advanced software development of 2D and 3D model visualization for TwinPrint, a dual-arm 3D bioprinting system for multi-material printing. *Mater Sci Addit Manuf,* 1(3): 19.

35. Lee JM, Sing SL, Yeong WY, 2020, Bioprinting of multimaterials with computer-aided design/computer-aided manufacturing. *Int J Bioprinting*, 6(1): 245.